Sánchez-Arriaga, G.; Pastor-Rodríguez, A.; Sanjurjo-Rivo, M.; Schmehl, R. (2019). A lagrangian flight simulator for airborne wind energy systems. *Applied Mathematical Modelling*, vol. 69, pp. 665-684.

DOI: https://doi.org/10.1016/j.apm.2018.12.016

A Lagrangian Flight Simulator for Airborne Wind Energy Systems

G. Sánchez-Arriaga[a,*], A. Pastor-Rodríguez[a], M. Sanjurjo-Rivo[a], R. Schmehl[b]

[a] *Bioengineering and Aerospace Engineering Department, Universidad Carlos III de Madrid, Avda de la Universidad 30, 28911, Leganés, Spain*
[b] *Delft University of Technology, Faculty of Aerospace Engineering, Kluyverweg 1, 2629 HS Delft, The Netherlands*

Abstract

A parallelized flight simulator for the dynamic analysis of airborne wind energy (AWE) systems for ground- and fly-generation configurations is presented. The mechanical system comprises a kite or fixed-wing drone equipped with rotors and linked to the ground by a flexible tether. The time-dependent control vector of the simulator mimics real AWE systems and it includes the length of the main tether, the geometry of the bridle, the torque of the motor controllers of the rotors, and the deflections of ailerons, rudder and elevator. The use of a lagrangian formulation with a minimal coordinate approach and discretizing the main tether as a chain of inelastic straight rods linked by ideal (dissipative-less) rotational joints, yielded a non-stiff set of ordinary differential equations free of algebraic constraints. Several verification tests, including a reel-in maneuver that admits an analytical solution, are presented. The efficiency of the parallelization with the number of tether segments, and trade-off analysis of the lagrangian and hamiltonian formulations are also considered. The versatility of the simulator is highlighted by analyzing two maneuvers that are relevant for AWE scenarios. First, the simulator is used to compute periodic figure-of-eight trajectories with an open-loop control law that varies the geometry of the kite's bridle, as frequently done in ground generation AWE systems. Second, an unstable equilibrium state of a tethered drone equipped with two rotors for energy

*Corresponding author: gonzalo.sanchez@uc3m.es

harvesting is stabilized by implementing a close-loop control strategy for the deflection of the control aerodynamic surfaces.

Keywords: `Kite Modeling, Lagrangian Systems, Kite Control`

Nomenclature

B	wingspan (m)
C	chord (m)
C_f	rotor thrust/drag coefficient
C_m	rotor torque coefficient
D_T	tether diameter (m)
E_T	tether Young's modulus (Pa)
g	gravitational acceleration (m/s^2)
$\boldsymbol{I}$	tensor of inertia (kgm^2)
L	length (m)
L_{T0}	initial tether length (m)
ℓ_R	dimensionless length of a rod
ℓ_B	dimensionless length of the bridle
M	mass (kg)
N_R	Number of rods
N_G	Number of rotors
$\boldsymbol{q_s}$	vector of degrees of freedom
$\boldsymbol{q_c}$	vector of control variables
$\boldsymbol{R}$	position vector (m)
S	Kite/drone surface (m^2)
$\boldsymbol{u}$	control vector
$\boldsymbol{V}$	velocity vector (m/s)

2

$\boldsymbol{x}$	state vector
$\boldsymbol{x}_i, \boldsymbol{y}_i, \boldsymbol{z}_i$	unit vectors of frame i
α	angle of attack (rad)
β	sideslip angle (rad)
δ	longitudinal angle of the bridle (rad)
η	lateral angle of the bridle (rad)
γ	elevation angle of a rod (rad)
φ	lateral angle of a rod (rad)
θ	pitch angle (rad)
ψ	yaw angle (rad)
ϕ	roll angle (rad)
λ	rotor angle (rad)
ν	rotor mounting angle (rad)
ρ	air density (kg/m^3)
ρ_T	tether density (kg/m^3)
$\boldsymbol{\Omega}$	angular velocity (rad/s)
τ	dimensionless time
ξ	dimensionless torque of a motor controller

3

Subscripts

E	Earth-fixed frame
G	generator/rotor
K	kite or drone
R	rods
T	tether
W	wind

Notation

Upper case	Physical variable
Lower case	Dimensionless variable
$s\alpha$	$sin\alpha$
$c\alpha$	$cos\alpha$

1. Introduction

The development of airborne wind energy (AWE) systems faces several challenges. Apart from safety issues, demonstration of autonomous and continuous operation over long periods of time, including take off and landing, are among the most important ones [1, 2]. In addition, the architecture of current technology demonstrators and their control laws should be optimized in order to increase the energy conversion efficiency. These demanding tasks inevitably need to make use of system simulators, some of them already shared with the research community [3, 4, 5, 6]. The performance of the simulators are conditioned by the choice of the model of the kite or drone, as well as the elastic or inelastic character of the tether, and the incorporation of the control variables in the dynamical system. As explained in the following, these choices affect critically the fidelity and computational efficiency of the simulators.

As highlighted in Ref. [7], most of past works on automated kite control used a point mass kite model (see for instance [8, 9, 10, 11]). Although such approximation is useful to get first estimations of some relevant variables such as the average power output, it is not sufficiently accurate for advanced analyses. The aerodynamic force acting on the kite depends on the kite attitude, a feature that is not captured by a point mass model. A kite model consisting of several connected point masses has been proposed [5]. An alternative is representing the kite as a rigid body [12, 13, 14, 15] which provides a good balance between accuracy and computational cost. Flexibility effects have been incorporated in kite flight simulators by using a multibody-system model reduction process [16].

The tether model is also relevant because it heavily affects the accuracy and the speed of the simulator. Tether models based on point masses linked by elastic springs and dampers [5, 17] can be easily implemented and they capture both flexibility and elasticity effects. However, due to their high stiffness, elastic tethers exhibit fast longitudinal waves of velocity $\sqrt{E_T/\rho_T}$, with E_T and ρ_T being the Young's modulus and the tether density, respectively. These waves are typically much faster than the transverse waves (vibrating string), which have

5

a velocity $\sqrt{T/A_T\rho_T}$, with T and A_T being the tether tension and cross section area. As a consequence, the equations of motion of elastic tethers have two different time scales and the use of implicit integrators become unavoidable. The stiffness problem disappears by using an inelastic tether model that captures flexibility effects, such as tether sagging, and removes completely the longitudinal fast oscillations. However, inelastic tethers introduce constraints, and a classical formalism for the equations of motion yields a mixed system of ordinary differential equations and nonlinear algebraic equations [18, 19]. For this reason, many studies on space tethers [20, 21, 22, 23] and kites [24, 12, 25, 13, 26, 15, 27] used a Lagrange's formalism based on minimal coordinates and Minakov's theory [28].

Most of previous works used simple models for the control inputs. For instance, the angle of attack [5, 25], the turn rate of the kite [10], and the lift coefficient and roll angle [11] were directly taken as control inputs or correlated through simple analytical laws. Although these hypotheses do not yield a self-consistent dynamical system, they simplify the dynamics notably and interesting results on kite control and stability were found. However, variables such as the angle of attack or the lift coefficient are not directly controlled in real AWE systems. Some of them have a winch on the ground station that reels in and out the main tether. They can also be equipped with a control unit, either suspended below the wing or on the ground station, that regulates the relative lengths of the lines of the kite bridle. Rigid wing AWES frequently have movable aerodynamic surfaces, like elevators, rudders, and ailerons.

This work presents a mathematical model for the simulation of AWE systems with the following characteristics: (i) the kite/drone is modeled as a rigid body, (ii) the tether is divided in segments, and each of them is modeled as a inelastic and straight rod, (iii) the equations of motion of the mechanical system are derived with Lagrange's formalism and they are not coupled with algebraic constraints, and (iv) tether reel-in and -out, bridle line control, and the deflection of the aerodynamic surfaces are incorporated rigorously in the model. The simulator can be used to study both ground-generation (GG) AWE systems, where

6

the tether tension is used to produce electrical energy with a drum-generator module at the ground, and fly-generation (FG) systems in which the kinetic energy of the wind is converted into electricity by onboard wind turbines. Each rotor, whose dynamic is also included self-consistently in the equations of motion, drives a permanent magnet motor/generator to generate power in normal operation or to drive propellers in a powered flight mode during take off and landing.

The manuscript is organized as follows. Section 2 presents the model that, in the most general case, includes a kite or a drone, a tether, a bridle, and an arbitrary number of rotors. Some cumbersome calculations related to the kinematics of the system and the aerodynamic forces are summarized in Appendix (A)-(C). Section 3 gives the explicit form of the equations of motion using both Lagrange and Hamilton's formalisms. The performance of the parallelized code and details about its verification are provided in Sec. 4. Some capabilities of the code are shown in Sec. 5, which presents simulation results of GG and FG systems with open and close loop control strategies, respectively. The conclusion of the work are summarized in Sec. 6. The code is a module of a more general package on AWE systems named LAKSA [29] and its MATLAB® version is available in a public repository [30]

2. System model

The notation, frame of references and methodology are similar to the ones used in previous works [26, 15]. The kite or drone mass M_K, the initial length of the tether L_{T0}, and the gravitational acceleration g are the characteristic parameters of the system from which dimensionless variables and parameters can be derived. Capital and lower case letters are used to denote variables with and without dimensions, respectively. For instance, we introduce the position vector of the center of mass of the kite $\boldsymbol{R}_K = L_{T0}\boldsymbol{r}_K$, its velocity $\boldsymbol{V}_K = \sqrt{gL_{T0}}\boldsymbol{v}_K$, its angular velocity $\boldsymbol{\Omega}_{KE} = \sqrt{g/L_{T0}}\boldsymbol{\omega}_{KE}$, the aerodynamic force $\boldsymbol{F}_A = M_K g \boldsymbol{f}_A$, and the aerodynamic moment about the center of mass $\boldsymbol{M}_A = M_K g L_{T0} \boldsymbol{m}_A$.

7

Derivatives with respect to the dimensionless time $\tau = t\sqrt{g/L_{T0}}$ are denoted with dots. Frames of references are indicated by the symbol S_A and their unit basis vectors by $\boldsymbol{x}_A, \boldsymbol{y}_A$, and $\boldsymbol{z}_A$.

We now describe the main elements of the most general version of the simulator and, at the end of this section, it is shown how GG and FG AWE systems naturally arise as particular cases in the model. The most complex mechanical system comprises: an inelastic but flexible tether, a kite or a drone, and an even number N_G of rotors. The modeling of such a complex dynamical system requires a set of simplifications and hypotheses. The following paragraphs provide a description of each element of the model and introduce the most important frames of reference used in the analysis. Concurrently, we will describe thoroughly the variables of the vectors

$$\boldsymbol{q}_s(\tau) = [\gamma_1, \dots \gamma_{N_R},\ \varphi_1, \dots \varphi_{N_R},\ \theta,\ \psi,\ \phi,\ \lambda_1, \dots \lambda_{N_G}]^T \tag{1}$$

$$\boldsymbol{q}_c(\tau) = [l_R,\ l_B,\ \delta,\ \eta,\ \xi_1,\ \dots \xi_{N_G},\ \delta_a,\ \delta_r,\ \delta_e]^T \tag{2}$$

where $\boldsymbol{q}_s$ and $\boldsymbol{q}_c$ contain the coordinates or degrees of freedom of the mechanical system and the control variables, respectively. The evolution of $\boldsymbol{q}_s$ is governed by the Lagrange equations (see Sec. 3) whereas $\boldsymbol{q}_c(\tau)$ is imposed externally and follows prescribed control laws. The precise meaning of each coordinate and control variable is presented along the following sections.

2.1. Drum-generator module and tether

The simulator considers a drum-generator module that can reel-in and reel-out the tether and controls the tether length $L_T(t)$. The modeling and dynamics of the winch are beyond the scope of this work (find a simple model in Ref. [5]). For convenience, we introduce an inertial frame of reference S_E with origin at the generator (point O_E), $\boldsymbol{z}_E$ pointing to the center of the Earth, and vectors $\boldsymbol{x}_E$ and $\boldsymbol{y}_E$ spanning the assumed flat Earth surface. The unit vector $\boldsymbol{x}_E$ points opposite to the wind velocity, which reads

$$\boldsymbol{V}_W(t) = -\sqrt{gL_{T0}}v_W(\tau)\boldsymbol{x}_E \tag{3}$$

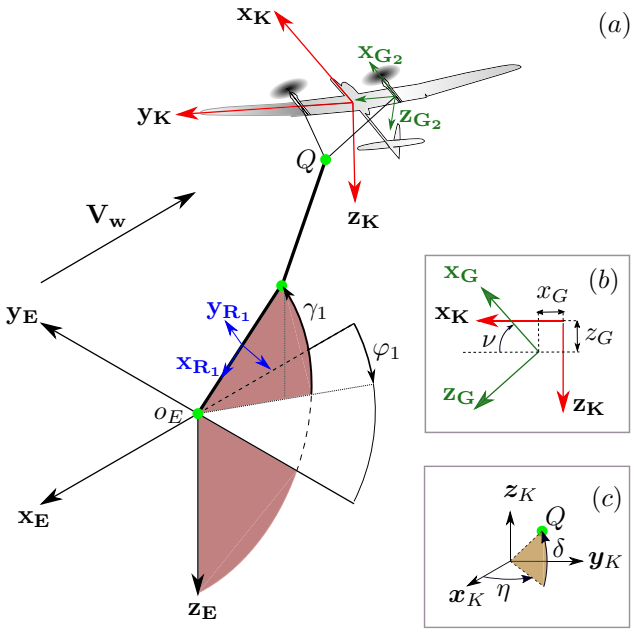

Figure 1: Frame of references and coordinates of the kite-tether system.

where $v_W(\tau)$ is a dimensionless function.

A tether with density ρ_T and diameter D_T connects the drum-generator module at the origin of S_E with the bridle of the kite at point Q. Our model incorporates tether flexibility effects but it ignores its elasticity, thus assuming that longitudinal perturbations travel at infinite velocity. This assumption does not affect significantly the reliability of the simulator, and is very convenient from a numerical point of view because it removes the fast longitudinal oscillations. Otherwise, the equation of motion would be stiff due to the existence of low frequency transversal oscillations and fast frequency longitudinal oscillations. Following previous works on space tethers [22, 23] and kites [15], the tether is divided into N_R segments. Each of them is modeled as a rigid and uniform rod linked by ideal joints (without dissipation) to the contiguous elements (the ground station, other rods, or the kite). All the tether segments or rods have the same instantaneous length $L_R(t)$ and mass $M_R(t)$, being the

9

total length of the tether $L_T(t) = N_R L_R(t)$. Two important dimensionless parameters related with the tether segments are the ratios

$$l_R(\tau) \equiv \frac{L_R(t)}{L_{T0}} \tag{4}$$

and

$$\frac{M_R}{M_K} = \sigma_T l_R(\tau), \qquad \sigma_T \equiv \frac{\rho_T \pi D_T^2 L_{T0}}{4 M_K} \tag{5}$$

According to these definitions, the initial dimensionless length of a tether segment is $l_R(0) = 1/N_R$. The function $l_R(\tau)$ is the first component of the vector with the control variables in Eq. (2). For tether segment i, we introduce a frame of reference S_{Ri} attached to it at any instant. Its origin O_{Ri} is at the middle of the tether segment and the unit vector $\boldsymbol{x}_{Ri}$ is along the direction defined by the segment itself. The components in S_{Ri} of the tensor of inertia of segment i about its center of mass are

$$\boldsymbol{I}_R(t) = M_K L_{T0}^2 \times \sigma_T l_R^3(\tau) \boldsymbol{\iota}_R, \qquad \boldsymbol{\iota}_R \equiv \begin{pmatrix} 0 & 0 & 0 \\ 0 & 1/12 & 0 \\ 0 & 0 & 1/12 \end{pmatrix} \tag{6}$$

Tether segments are infinitely thin, and just two angles are enough to define their orientation. Our model uses the lateral angles φ_i and the elevation angles γ_i defined in Fig. 1), which correspond to the first $2N_R$ components of the vector of coordinates in Eq. (1). Vector components in S_E and S_{Ri} are related by the rotation matrix $\boldsymbol{R}_i^{RE}$ that depends on the angles φ_i and γ_i [see Eq. (A.1)]. The normalized position vector of the center of mass of segment i can also be written as a function of these angles

$$\boldsymbol{r}_{Ri} = -l_R \sum_{j=1}^{i} e_j \left[c\gamma_j \left(c\varphi_j \boldsymbol{x}_E + s\varphi_j \boldsymbol{y}_E \right) + s\gamma_j \boldsymbol{z}_E \right] \tag{7}$$

where the factors e_j, which will always appear inside a sum in this study, are equal to $e_j = 1/2$ for j equal to the maximum index of the summation [$j = i$ in Eq. (7)], and $e_j = 1$ otherwise ($j < i$). The absolute velocity, i.e. the one found by an observer at S_E, is given by $\boldsymbol{v}_{Ri} = d\boldsymbol{r}_{Ri}/d\tau \mid_{S_E}$. As shown in Appendix

10

B, such a vector can be written as

$$\boldsymbol{v}_{Ri} = \frac{d\boldsymbol{r}_{Ri}}{d\tau} \mid_{S_E} = \boldsymbol{S}_{Ri}\dot{\boldsymbol{q}}_s + \boldsymbol{C}_{Ri}\dot{\boldsymbol{q}}_c \tag{8}$$

where $\boldsymbol{S}_{Ri}$ and $\boldsymbol{C}_{Ri}$ are two matrices that depend on $\boldsymbol{q}_s$ and $\boldsymbol{q}_c$ (but not on their τ-derivatives). Similarly, the normalized angular velocity of a frame S_{Ri} with respect to S_E is

$$\boldsymbol{\omega}_{Ri} = \boldsymbol{W}_{Ri}\dot{\boldsymbol{q}}_s \tag{9}$$

with $\boldsymbol{W}_{Ri}$ being a matrix given in Appendix B. Interestingly, $\boldsymbol{\omega}_{Ri}$ does not depend on $\dot{\boldsymbol{q}}_c$.

2.2. Bridle and kite/drone

The kite or drone, with mass M_K, chord C, wingspan B, and surface S, is connected to the main tether at point Q by a set of lines, which are commonly referred as bridle (see Fig. 1). The dimensionless position vector of point Q is a function of all the φ_i and γ_i and it reads

$$\boldsymbol{r}_Q = -l_R \sum_{j=1}^{N_R} \left[c\gamma_j \left(c\varphi_j \boldsymbol{x}_E + s\varphi_j \boldsymbol{y}_E \right) + s\gamma_j \boldsymbol{z}_E \right] \tag{10}$$

The lengths and masses of the bridle's lines are very small if compared with the ones of the main tether, and these lines typically acquire a straight shape due to the high tension. For these reasons, our model substitutes the lines of the bridle by a set of massless rods. Moreover, under such assumption, the details of the bridle, like the number of lines or the precise location of their attachment points at the kite, are not needed. The lines of the bridle impose a geometrical constraint and just the relative position between point Q and the center of mass of the kite O_K is relevant, i.e:

$$\frac{\overline{QO_K}}{L_{T0}} = -l_B \left(c\delta c\eta \boldsymbol{x}_K + c\delta s\eta \boldsymbol{y}_K + s\delta \boldsymbol{z}_K \right), \tag{11}$$

where $l_B(\tau)$, $\delta(\tau)$, and $\eta(\tau)$, are three known functions. According to Eq. (11) and the lower inset of Fig. 1, l_B is the normalized distance between O_K and Q, and δ and η are two angles that determine the position of Q inside and

11

outside the plane of symmetry of the kite, respectively. The evolutions of these variables, which are part of the vector with the control variables in Eq. (2), are imposed by the kite control unit that reels-in and reels-out the lines of the bridle.

Vectors $\boldsymbol{x}_K$, $\boldsymbol{y}_K$, and $\boldsymbol{z}_K$ in Eq. (11) form a basis of the frame of reference S_K with origin at the center of mass of the kite (O_K). Axes $O_K x_K$ and $O_K z_K$ belong to the plane of symmetry of the kite and axis $O_K x_K$ points forward in normal flight attitude (see Fig. 1). As usual in flight mechanics, the yaw (ψ), pitch (θ) and roll (ϕ) angles are used to orientate frame S_K with respect to S_E. These three variables are included in the vector of coordinates in Eq. 1 and also appear in the rotation matrix that relate vector components in the S_E and S_K frames [see Eq. A.2]. The components in S_K of the tensor of inertia of the kite about O_K then takes the following form:

$$\boldsymbol{I}_K = M_K L_{T0}^2 \boldsymbol{\iota}_K \quad \iota_K \equiv \begin{pmatrix} \iota_{xx} & 0 & \iota_{xz} \\ 0 & \iota_{yy} & 0 \\ \iota_{xz} & 0 & \iota_{zz} \end{pmatrix} \tag{12}$$

with ι_{xx}, ι_{yy}, ι_{zz}, and ι_{xz} four constants that depend on the geometry and mass distribution of the kite.

The normalized position vector of the center of mass of the kite is easily found by combining Eqs. (10) and (11) as follows

$$\boldsymbol{r}_K = \boldsymbol{r}_Q + \frac{\overline{QO_K}}{L_{T0}}, \tag{13}$$

and the absolute dimensionless velocity of the kite, $\boldsymbol{v}_K = d\boldsymbol{r}_K/d\tau\,|_{S_E}$, reads

$$\boldsymbol{v}_K = \boldsymbol{S}_K \dot{\boldsymbol{q}}_s + \boldsymbol{C}_K \dot{\boldsymbol{q}}_c \tag{14}$$

with $\boldsymbol{S}_K$ and $\boldsymbol{C}_K$ given in Appendix B.2. The normalized angular velocity of the kite with respect to the inertial frame S_E

$$\boldsymbol{\omega}_K = \boldsymbol{W}_K \dot{\boldsymbol{q}}_s \tag{15}$$

is also independent of the τ-derivative of $\boldsymbol{q}_c$ (see Appendix B.2).

12

2.3. On board rotors

In the case of FG AWES, the model also includes N_G rotors that are distributed symmetrically with respect to the plane of symmetry of the kite. Each rotor is taken as a rigid body made of a thin shaft and three blades. The two dimensionless parameters characterizing the rotors are

$$\sigma_G \equiv \frac{M_G}{M_K}, \quad l_G \equiv \frac{R_G}{L_{T0}} \tag{16}$$

with M_G the total mass of the rotor and R_G the length of each blade. Subscript G has been used to remind that in normal operation the rotors acts as generators. The centers of mass of the rotors, at points O_{Gj} with $j = 1, .., N_G$, are at fixed locations for an observed linked to the kite. We then can write

$$\frac{\overline{O_K O_{Gj}}}{L_{T0}} = x_{Gj}\boldsymbol{x}_K + y_{Gj}\boldsymbol{y}_K + z_{Gj}\boldsymbol{z}_K \tag{17}$$

where x_{Gj}, y_{Gj}, and z_{Gj} are known constants. The shafts of the rotors are contained in planes that are parallel to the plane of symmetry of the kite but they all form a constant angle ν with $\boldsymbol{x}_K$ (see Fig. 1b). For each rotor with subscript j, we introduce a frame of reference S_{Gj} with origin at O_{Gj}, and axes $O_{Gj}x_{Gj}$ and $O_{Gj}y_{Gj}$ along the directions of the shaft and one of the blades, respectively. Since the axes of this frame are principal axes of inertial, the components in S_{Gj} of the tensor of inertial of the rotor about its center of mass are

$$\boldsymbol{I}_G = M_K L_{T0}^2 \times \sigma_G l_G^2 \; \boldsymbol{\iota}_G, \qquad \boldsymbol{\iota}_G = \begin{pmatrix} 1/3 & 0 & 0 \\ 0 & 1/6 & 0 \\ 0 & 0 & 1/6 \end{pmatrix} \tag{18}$$

where we assumed that the blades are uniform, straight, and infinitely thin and also ignored the mass of the shaft as compared to the mass of a blade.

From the position vectors of the centers of mass of the rotors

$$\boldsymbol{r}_{Gj} = \boldsymbol{r}_K + \frac{\overline{O_K O_{Gj}}}{L_{T0}}, \tag{19}$$

one can also compute the velocities of their center of mass with respect to S_E

$$\boldsymbol{v}_{Gj} = \frac{d\boldsymbol{r}_{Gj}}{d\tau} \; |_{S_E} = \boldsymbol{S}_{Gj}\dot{\boldsymbol{q}}_s + \boldsymbol{C}_{Gj}\dot{\boldsymbol{q}}_c \tag{20}$$

13

where $j = 1, \ldots, N_G$. Matrices $\boldsymbol{S}_{Gj}$ and $\boldsymbol{C}_{Gj}$ are given in Appendix B.3. Each rotor has one degree of freedom that corresponds to its rotation angle $\lambda_j(\tau)$ about the shaft. These angles are included in the vector of coordinates of the simulator [see Eq. (1)]. The angular velocity of the rotors with respect to the Earth frame is

$$\boldsymbol{\omega}_{G_j} = \boldsymbol{\omega}_K + \dot{\lambda}_j \boldsymbol{x}_{Gj} = \boldsymbol{W}_{Gj} \dot{\boldsymbol{q}}_s \tag{21}$$

The explicit form of matrix $\boldsymbol{W}_{Gj}$ is given in Appendix B.3.

2.4. Onboard controls

In some GG systems, such as the one developed in TU Delft, the control is carried out by the already described drum-generator module and the bridle control unit, which set the values of l_R, and l_B, δ, and η, respectively. However, there are other configurations, such as the FG system by Makani, with different control actuators. In order to cover all the possible cases and combinations, we now introduce motor controllers of the rotors and the movable aerodynamic surfaces: ailerons, elevators, and rudder. For simplicity, the equivalent circuit model of the motor controller that involves other variables such as current, voltage, and motor parameters are not included in the simulator. Our model incorporates the motor controller by adding a normalized torque $\boldsymbol{m}_{CG}^j$ acting upon each rotor j. Such a torque reads

$$\boldsymbol{m}_{CG}^j = -\xi_j(\tau) \boldsymbol{x}_{Gj} \tag{22}$$

where ξ_j is a dimensionless function imposed by the motor controller. Therefore, the following reaction dimensionless torque acts upon the kite

$$\boldsymbol{m}_{CK} = -\sum_{j=1}^{N_G} \boldsymbol{m}_{CG}^j \tag{23}$$

On the other hand, the aerodynamic model of the kite or drone explained in Appendix C depends on the deflections of the ailerons $\delta_a(\tau)$, elevator $\delta_e(\tau)$, and rudder $\delta_r(\tau)$.

For the most general configuration of the simulator, the vectors with the coordinates and the control variables have dimensions equal to $N_s = 2N_R + 3 + N_G$

14

(tether segments + kite + rotors) and $N_c = 1 + 3 + N_G + 3$ (tether + bridle + motor controller torques + aerodynamic surface deflection), respectively. Therefore, the simulator is suitable for most of the AWE systems under development. For instance, the GG AWES by TU Delft is obtained as a particular case of the simulator if all the variables related with the rotors and the movable aerodynamic surfaces, are ignored. On the other hand, the normal operation of Makani's prototype, which is a FG system, can be simulated by setting constant values to the control variable l_R, l_B, δ, and η, and giving time histories for $\xi_j(\tau)$, $\delta_a(\tau)$, $\delta_e(\tau)$, and $\delta_r(\tau)$. During its take-off and landing l_R is not constant but it would follow the control law imposed by the drum module on the ground. The systems of other companies (Ampyx Power, Kite Power Systems, ...) are also subcases of our simulator.

3. Equations of motion

3.1. Lagrangian formulation

The set of equations that governs $\boldsymbol{q}_s(\tau)$ for a given control law $\boldsymbol{q}_c(\tau)$ are

$$\frac{\mathrm{d}}{\mathrm{d}\tau}\left(\frac{\partial \mathcal{L}}{\partial \dot{q}_{sm}}\right) - \frac{\partial \mathcal{L}}{\partial q_{sm}} = Q_m \tag{24}$$

with $m = 1, ..., N_s$. Due to the large number of involved bodies in the model, the computation of the normalized lagrangian function $\mathcal{L}$ and the generalized force components Q_m is cumbersome. The lagrangian $\mathcal{L} = \mathcal{T} - \mathcal{U}$ involves the total normalized kinetic energy of the system

$$\begin{aligned}\mathcal{T} =& \frac{1}{2}\left[\sigma_T l_R \sum_{i=1}^{N_R}\left(v_{Ri}^2 + l_R^2 \boldsymbol{\omega}_{Ri}^T \cdot \boldsymbol{\iota}_R \cdot \boldsymbol{\omega}_{Ri}\right) + v_K^2 + \right.\\ & \left. \boldsymbol{\omega}_K^T \cdot \boldsymbol{\iota}_K \cdot \boldsymbol{\omega}_K + \sigma_G \sum_{i=1}^{N_G}\left(v_{Gi}^2 + l_G^2 \boldsymbol{\omega}_{Gi}^T \cdot \boldsymbol{\iota}_G \cdot \boldsymbol{\omega}_{Gi}\right)\right]\end{aligned} \tag{25}$$

The results presented in Sec. 2 make the computation of the lagrangian function straightforward. Substituting Eqs. (8), (14), and (20) for the velocities and Eqs. (9), (15), and (21) for the angular velocities in Eq. (25) yields

$$\mathcal{T} = \frac{1}{2}\left(\dot{\boldsymbol{q}}_s^T \boldsymbol{M}_s \dot{\boldsymbol{q}}_s + 2\dot{\boldsymbol{q}}_s^T \boldsymbol{M}_{sc} \dot{\boldsymbol{q}}_c + \dot{\boldsymbol{q}}_c^T \boldsymbol{M}_c \dot{\boldsymbol{q}}_c\right) \tag{26}$$

15

with

$$\begin{aligned}\boldsymbol{M}_s =&\sigma_T l_R \sum_{i=1}^{N_R} \left(\boldsymbol{S}_{Ri}^T \boldsymbol{S}_{Ri} + l_R^2 \boldsymbol{W}_{Ri}^T \boldsymbol{\iota}_R \boldsymbol{W}_{Ri}\right) + \boldsymbol{S}_K^T \boldsymbol{S}_K + \\ &\boldsymbol{W}_K^T \boldsymbol{\iota}_K \boldsymbol{\Omega}_K + \sigma_G \sum_{i=1}^{N_G} \left(\boldsymbol{S}_{Gi}^T \boldsymbol{S}_{Gi} + l_G^2 \boldsymbol{W}_{Gi}^T \boldsymbol{\iota}_G \boldsymbol{W}_{Gi}\right) \end{aligned} \tag{27}$$

$$\boldsymbol{M}_{sc} =\sigma_T l_R \sum_{i=1}^{N_R} \boldsymbol{S}_{Ri}^T \boldsymbol{C}_{Ri} + \boldsymbol{S}_K^T \boldsymbol{C}_K + \sigma_G \sum_{i=1}^{N_G} \boldsymbol{S}_{Gi}^T \boldsymbol{C}_{Gi} \tag{28}$$

$$\boldsymbol{M}_c =\sigma_T l_R \sum_{i=1}^{N_R} \boldsymbol{C}_{Ri}^T \boldsymbol{C}_{Ri} + \boldsymbol{C}_K^T \boldsymbol{C}_K + \sigma_G \sum_{i=1}^{N_G} \boldsymbol{C}_{Gi}^T \boldsymbol{C}_{Gi} \tag{29}$$

The lagrangian function of the system also involves the normalized potential energy

$$\mathcal{U} = -\left(\sigma_T l_R \sum_{i=1}^{N_R} \boldsymbol{r}_{Ri} + \boldsymbol{r}_K + \sigma_G \sum_{i=1}^{N_G} \boldsymbol{r}_{Gi}\right) \cdot \boldsymbol{z}_E \tag{30}$$

Constraints forces among tether segments (tether tensions), between the kite and the bridle, and the kite and the rotors, do not appear explicitly in the equations of motion because the joints are assumed ideal. This is the main advantage of the lagrangian formulation with a minimal coordinate approach. However, the torque of the motor controller and the aerodynamic forces and torques upon all the elements of the system should be included in the generalized forces

$$\begin{aligned}Q_m =&\sum_{i=1}^{N_R} \boldsymbol{f}_{AR}^i \cdot \frac{\partial \boldsymbol{v}_{Ri}}{\partial \dot{q}_{sm}} + \boldsymbol{f}_{AK} \cdot \frac{\partial \boldsymbol{v}_K}{\partial \dot{q}_{sm}} + \boldsymbol{m}_K \cdot \frac{\partial \boldsymbol{\omega}_K}{\partial \dot{q}_{sm}} \\ &\sum_{i=1}^{N_G} \left[\boldsymbol{f}_{AG}^i \cdot \frac{\partial \boldsymbol{v}_{Gi}}{\partial \dot{q}_{sm}} + \boldsymbol{m}_G^i \cdot \frac{\partial \boldsymbol{\omega}_{Gi}}{\partial \dot{q}_{sm}}\right] \end{aligned} \tag{31}$$

with $m = 1 \ldots N_s$ and $\boldsymbol{f}_{AR}^i$, $\boldsymbol{f}_{AK}$, and $\boldsymbol{f}_{AG}^i$ the normalized aerodynamic forces acting on the tether segments, the kite, and the rotors,respectively. Equation (31) neglects the aerodynamic torque on the rods. However, it considers the total torque upon the kite $\boldsymbol{m}_K = \boldsymbol{m}_{AK} + \boldsymbol{m}_{CK}$ and the rotors $\boldsymbol{m}_G^i = \boldsymbol{m}_{AG}^i + \boldsymbol{m}_{CG}^i$ that involve their aerodynamic torques and the one coming from the motor controllers. These forces and torques are functions of the coordinates and the control variables, and their explicit forms are given in Appendix C).

16

Substituting these results for the lagrangian and the generalized forces in Eq. (24) leads to the following set of second order differential equations

$$\begin{aligned} M_{smj}\ddot{q}_{sj} + M_{scmj}\ddot{q}_{cj} + \frac{\partial M_{smj}}{\partial q_{sk}}\dot{q}_{sk}\dot{q}_{sj} + \\ \frac{\partial M_{scmj}}{\partial q_{sk}}\dot{q}_{sk}\dot{q}_{cj} + \frac{\partial M_{smj}}{\partial q_{ck}}\dot{q}_{ck}\dot{q}_{sj} + \frac{\partial M_{scmj}}{\partial q_{ck}}\dot{q}_{ck}\dot{q}_{cj} - \\ \frac{1}{2}\left(\frac{\partial M_{sjk}}{\partial q_{sm}}\dot{q}_{sj}\dot{q}_{sk} + 2\frac{\partial M_{scjk}}{\partial q_{sm}}\dot{q}_{sj}\dot{q}_{ck} + \frac{\partial M_{cjk}}{\partial q_{sm}}\dot{q}_{cj}\dot{q}_{ck}\right) \\ + \frac{\partial \mathcal{U}}{\partial q_{sm}} = Q_m \end{aligned} \tag{32}$$

with $m = 1 \dots N_s$.

3.2. Hamiltonian formulation

Most of previous works on kite dynamics use classical mechanics or lagrangian formulation. However, Hamilton's equations have several interesting features, and can be straightforwardly obtained from the Lagrange equations. We now show the main steps to find the equations of motion of the system by using Hamiltonian formulation and discuss their peculiarities. The matrix and index notation introduced in previous sections make the transformation from lagrangian to hamiltonian formulations very simple.

After computing the momenta by differentiating the lagrangian function with respect to the generalized velocities, i.e.:

$$\boldsymbol{p} = \frac{\partial \mathcal{L}}{\partial \dot{\boldsymbol{q}}_s} = \boldsymbol{M}_s\dot{\boldsymbol{q}}_s + \boldsymbol{M}_{sc}\dot{\boldsymbol{q}}_c, \tag{33}$$

one finds hamiltonian function

$$\mathcal{H} \equiv \dot{\boldsymbol{q}}_s^T \cdot \boldsymbol{p} - \mathcal{L} = \frac{1}{2}\left(\dot{\boldsymbol{q}}_s^T\boldsymbol{M}_s\dot{\boldsymbol{q}}_s - \dot{\boldsymbol{q}}_c^T\boldsymbol{M}_c\dot{\boldsymbol{q}}_c\right) + \mathcal{U} \tag{34}$$

We now eliminate $\dot{\boldsymbol{q}}_s$ by using Eq. (33) and write the hamiltonian as

$$\mathcal{H}\left(\boldsymbol{q}_s, \boldsymbol{p}\right) = \frac{1}{2}\left[\boldsymbol{p}^T\boldsymbol{H}_p\boldsymbol{p} - 2\dot{\boldsymbol{q}}_c^T\boldsymbol{H}_{cp}\boldsymbol{p} + \dot{\boldsymbol{q}}_c^T\boldsymbol{H}_c\dot{\boldsymbol{q}}_c\right] + \mathcal{U} \tag{35}$$

with $\boldsymbol{H}_p = \boldsymbol{M}_s^{-1}$, $\boldsymbol{H}_{cp} = \boldsymbol{M}_{sc}^T\boldsymbol{M}_s^{-1}$ and $\boldsymbol{H}_c = \boldsymbol{M}_{sc}^T\boldsymbol{M}_s^{-1}\boldsymbol{M}_{sc} - \boldsymbol{M}_c$. The explicit

17

form of Hamilton's equations

$$\frac{d\boldsymbol{q}_s}{d\tau} = \frac{\partial \mathcal{H}}{\partial \boldsymbol{p}}, \tag{36}$$

$$\frac{d\boldsymbol{p}}{d\tau} = -\frac{\partial \mathcal{H}}{\partial \boldsymbol{q}_s} + \boldsymbol{Q} \tag{37}$$

is

$$\frac{dq_{sm}}{d\tau} = H_{pmj} p_j - H_{cpjm} \dot{q}_{cj} \tag{38}$$

$$\frac{dp_m}{d\tau} = -\frac{1}{2}\left[\frac{H_{pij}}{\partial q_{sm}} p_i p_j - 2\frac{H_{cpij}}{\partial q_{sm}} \dot{q}_{ci} p_j + \frac{H_{cij}}{\partial q_{sm}} \dot{q}_{ci} \dot{x}_{cj}\right] - \frac{\partial \mathcal{U}}{\partial q_{sm}} + Q_m \tag{39}$$

with $m = 1 \cdots N_s$. The evolution of the hamiltonian can be obtained by integrating the following equation

$$\frac{d\mathcal{H}}{d\tau} = \dot{\boldsymbol{q}}_s^T \cdot \boldsymbol{Q} - \frac{\partial \mathcal{L}}{\partial \tau} \tag{40}$$

where $\boldsymbol{Q}$ is a column vector with the components of the generalized forces. If the control variables are constant, then the Hamiltonian coincides with the mechanical energy ($\mathcal{H} = \mathcal{T} + \mathcal{U}$) and thus $\partial \mathcal{L}/\partial t = 0$. For such a particular case, Eq. (40) shows that the change of the mechanical energy of the system is equal to the work done by the non-conservative forces.

An important feature of the equations of motion is that the variables λ_i, i.e. the angular coordinates of the blades of the rotors, do not appear explicitly in the right hand side of Eqs. (38)-(39). A priori, there are only two places where λ_i could potentially appear. First, one can check that the term $\boldsymbol{\omega}_{Gi}^T \cdot \boldsymbol{\iota}_G \cdot \boldsymbol{\omega}_{Gi}$ in Eq. (26) does not involve λ_i thanks to the special form of the tensor $\boldsymbol{\iota}_G$ that has $\boldsymbol{\iota}_G(2,2) = \boldsymbol{\iota}_G(3,3)$. Therefore, the lagrangian and the hamiltonian functions are independent of λ_i. Second, the contribution of the rotors to the generalized force does not introduce an explicit dependence with λ_i because $\boldsymbol{f}_{AG}^i$ and $\boldsymbol{m}_G^i$ are along $\boldsymbol{x}_{Gi}$ and the first row of the rotation matrix $\boldsymbol{R}_i^{GK}$ is independent of λ_i. For this reason, the final implementation of our simulator does not include the variables λ_i in the state vector and the last N_G equations of (36), which are

18

decoupled from the others, are ignored. Such approach is very convenient from a numerical point of view, because the dynamics of the blades is much faster than the ones of the kite and the tether. Including the evolution equations for λ_i would yield a stiff set of equations, leading to worse computational performance.

4. Implementation, verification and performance of the simulator

The equations of motion, i.e. Eqs. (32) or (38)-(39), can be written as

$$\frac{d\boldsymbol{x}}{d\tau} = \boldsymbol{f}\left[\boldsymbol{x}, \boldsymbol{u}\left(\tau\right)\right]. \tag{41}$$

where $\boldsymbol{x} = [\hat{\boldsymbol{q}}_s \;\; \dot{\boldsymbol{q}}_s]$ (or $\boldsymbol{x} = [\hat{\boldsymbol{q}}_s \;\; \boldsymbol{p}]$) is the state vector, $\hat{\boldsymbol{q}}_s = [\gamma_1, \; \ldots \gamma_{N_R}, \; \varphi_1, \; \ldots \; \varphi_{N_R}, \; \theta, \; \psi, \; \phi]^T$ is a vector with the coordinated or degrees of freedom of the system except the λ_i, and $\boldsymbol{u} = [\boldsymbol{q}_c \;\; \dot{\boldsymbol{q}}_c \;\; \ddot{\boldsymbol{q}}_c]$ is the control vector. Therefore, the total dimension of this system is $2 \times (N_R + 3) + N_G$. Given a set of initial conditions, the numerical integration of the systems involves the computation of the tensors in Eq. (32) or (38)-(39) at each time step. Although the analytical expressions of the gradients of $\boldsymbol{M}_s$, $\boldsymbol{M}_{sc}$, and $\boldsymbol{M}_c$ have been implemented in the code, such a computation is the most demanding operation from a computational point of view, especially when the number of tether segments is large. We also remark that the control vector contains the first and second derivatives of $\boldsymbol{q}_c$. Although we did not encounter any difficulty in the examples of this work, special care should be taken during numerical integrations if the rates of change of the controls are very high.

The equations of motion have been implemented in two separate simulators, aimed at different purposes. The first one is a MATLAB®-based code that runs on a single processor. Such a simulator is available in a public repository [30] and is appropriate for academic purposes. The second simulator has been implemented in Fortran and uses shared memory multiprocessing (OpenMP) for the computation of the gradients of $\boldsymbol{M}_s$, $\boldsymbol{M}_{sc}$, and $\boldsymbol{M}_c$, as well as equation assembly. Both implementations can integrate the lagrangian and the hamiltonian forms of the equations of motion.

19

4.1. Performance and parallel scalability

A relevant metric to measure the performances of the parallelized Fortran simulator is the required time that is necessary to evaluate the right hand side of Eq. (41). The time consumed in the numerical integration of the equations of motion is directly related to this metric, and it is easier to test it with identical conditions. The analysis was performed varying the numbers of tether segments and number of processors. The computations were carried out on a dedicated cluster with 44 Intel Xeon E5-2699 v4 processors at 2.20 GHz. Tests consist on the computation of the right hand side of Eqs. (41) one thousand times for exactly the same inputs. We took a batch of one thousand states vectors and instants obtained during a transient trajectory with initial condition equal to the equilibrium state of the system plus a small perturbation.

Figure 2 shows the computational time by using lagrangian formulation. If the number of tether segments is small, then it is convenient to use a single thread because the parallelization deteriorates the performance. Parallelization is advantageous when flexibility effects (tether sagging) are important and a high number of tether segments are needed to capture properly tether dynamics. In this regards, the code exhibits a good scalability and the computational time is almost halved when the number of threads is doubled for a given number of tether segments.

When comparing lagrangian [Eqs. (32)] and hamiltonian [Eqs. (38)-(39)] formulations, one readily find that the latter involves a smaller number of tensors. In particular, in Eqs. (38)-(39) there are no tensor involving the partial derivatives of matrices with respect to the control vector. From a computational point of view, this constitutes a cost saving as compared to the lagrangian formulation. However, in order to check the quality of the numerical integration, one typically add Eq. (40) to the system of equations. Since the term $\partial\mathcal{L}/\partial t$ involves the calculation of the partial derivatives of some matrices with respect the control, the Hamiltonian formulation does not allow to save significant computational resources in practical implementations. Actually, as shown in Fig. 3, the required time to evaluate one thousand times the right-hand side of the

20

equations of motion with Hamiltonian formulation is typically a ten percent higher than the lagrangian one.

Taking into account that the chosen metric is an indirect indicator of the integration performance, the above conclusion does not mean necessarily than the lagrangian formulation is more efficient. Using our MATLAB® simulator, we performed two numerical integrations with the same initial condition, integrator tolerance, and explicit Runge-Kutta integrator with variable time step. The integration with the Hamiltonian formulation was a 20% faster because the numerical integrator made a smaller number of evaluations of the right-hand side. Moreover, the difference between the Hamiltonian provided by Eqs. (34) and (40) revealed that the numerical stability of the the Hamiltonian formulation is better. Therefore, the best performing simulator depends on the particular case of study and, beyond performance, both formulations exhibit advantages and drawbacks.

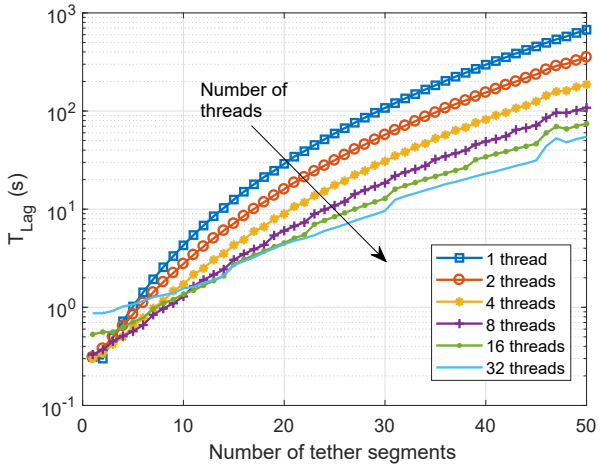

Figure 2: Computational time versus number of tether segments.

4.2. Code verification

The following tests were designed and carried out to verify the implementation of the code: (i) the analytical computations of the gradients of $\boldsymbol{M}_s$, $\boldsymbol{M}_{sc}$,

21

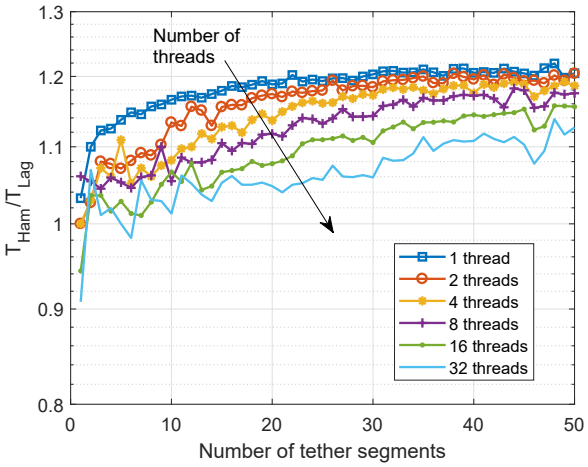

Figure 3: Hamiltonian-to-Lagrangian computational time ratio.

and $\boldsymbol{M}_c$ have been compared against numerical calculations using finite difference methods, (ii) for $N_R = 1$ and $\sigma_T \to 0$, i.e., a single straight and massless tether, we checked that the simulator recovers the results of Ref. [26] for both longitudinal and lateral directional motions, (iii) for $N_R = 5$ and longitudinal dynamics ($\varphi_i = \dot{\varphi}_i = \eta = 0$), the results of the simulator agree with the ones presented in Ref. [15], (iv) for every calculation the accomplishment of Eq. (40) is monitored, and (v) the results of the simulations were postprocess to verify that the dynamics of all the rigid bodies (tether segments, kite, and rotors) satisfy the Newton's laws for linear and angular momentum. The latest test provides the constraint forces and also proves the consistency of our lagrangian simulator with classical mechanics formulation.

In addition to the previous tests, the implementation of the code has been verified by comparing the simulation results with a simple analytical solution. We consider a kite or drone without rotors ($N_G = 0$), and linked to the ground by a single ($N_R = 1$), massless ($\sigma_T = 0$) and infinitely thin ($\chi_R = 0$) tether. There is no wind, and the length of the tether decreases according to the law $l_R = 1 + v_{in}\tau$, with v_{in} a negative constant representing the dimensionless reel-in velocity. If we look for symmetric ($\varphi_1 = \phi = \psi = 0$) and stationary ($\dot{\boldsymbol{q}}_s = 0$)

22

solutions, then one finds $\boldsymbol{v}_K = \boldsymbol{v}_K^A = v_{in}\left(\cos\gamma_1 \boldsymbol{i}_E + \sin\gamma_1 \boldsymbol{z}_E\right)$ and $\alpha = \theta + \gamma_1$. A simple force and torque balance for the kite gives

$$\mu v_{in}^2 \left[C_x \cos\theta + C_z \sin\theta\right] + T\cos\gamma_1 = 0 \tag{42}$$

$$\mu v_{in}^2 \left[C_z \cos\theta - C_x \sin\theta\right] + T\sin\gamma_1 + 1 = 0 \tag{43}$$

$$\mu\epsilon_c v_{in}^2 C_m - T l_B \sin\left(\alpha - \delta\right) = 0 \tag{44}$$

with $C_x(\alpha) = C_{x0} + C_{x\alpha}\alpha$, $C_z(\alpha) = C_{z0} + C_{z\alpha}\alpha$, $C_m(\alpha) = C_{m0} + C_{m\alpha}\alpha$, and T the dimensionless tether tension. For a given reel-in rate, v_{in}, Eqs. (42)-(44) provides the equilibrium pitch angle θ, and tether elevation angle γ_1 and tension T. These equations are non-linear, but a simple analytical analysis can be performed to uncover the physics of the reel-in maneuver. We first note that at the particular reel-in velocity

$$v_{in}^* = \left[\mu\left(C_x^* \sin\theta^* - C_z^* \cos\theta^*\right)\right]^{-1/2}, \tag{45}$$

the tether tension vanishes and the state variables are $\theta^* = -\arctan\left(C_x^*/C_z^*\right)$ and $\gamma^* = \alpha^* - \theta^*$ with $\alpha^* = -C_{m0}/C_{m\alpha}$, $C_x^* = C_x\left(\alpha^*\right)$, $C_z^* = C_z\left(\alpha^*\right)$. In order to investigate the reel-in maneuver with velocities close to v_{in}^*, we substitute in Eqs. (42)-(44) the expansions $v_{in} = v_{in}^* + \tilde{v}_{in}$, $\alpha = \alpha^* + \tilde{\alpha}$, $\theta = \theta^* + \tilde{\theta}$, $T = \tilde{T}$, and drop quadratic terms in the variables with tilde (assumed to be small). After some cumbersome calculations, one finds

$$\tilde{T} = \frac{\mu\epsilon_c C_{m\alpha} v_{in}^{*2}}{l_B \sin\left(\alpha^* - \delta\right)}\tilde{\alpha} \tag{46}$$

$$\tilde{\alpha} = -\frac{2\tilde{v}_{in}}{v_{in}^*}\left[\frac{C_z^{*2} + C_x^{*2}}{C_x^* C_{x\alpha} + C_z^* C_{z\alpha} + \frac{\epsilon_c C_{m\alpha} C_z^* \sin\gamma^*}{l_B \sin(\alpha^* - \delta)\cos\theta^*}}\right] \tag{47}$$

Equations (46) and (47) show that the dependence of the tension with the reel-in velocity for this special non-accelerated solution is intricate. In particular, the aerodynamic parameters and the geometry of the bridle (l_B and δ) play an important role [see angle δ in the denominator of Eq. (47)] and the tether tension does not increases necessarily with the modulus of v_{in}. These features are highlighted in Fig. 4 that shows the normalized tension, angle of attack and elevation angle of the tether computed from Eqs. (42)-(44) for $\delta = 5°$

23

and $\delta = 25°$. The v_{in}-range yielding $T < 0$ is not physical because the tether would be under compression. For $\delta = 5°$ ($\delta = 25°$) the tether tension increases (decreases) with $\mid v_{in} \mid$.

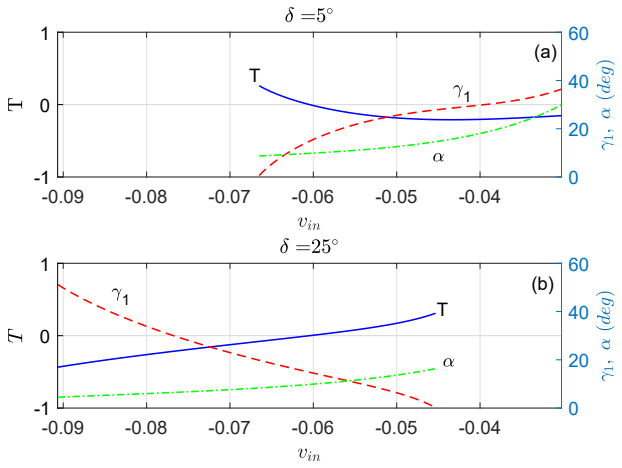

Figure 4: Panels (a) and (b) show the normalized tension (left) and the elevation angle and angle of attack (right) versus the reel-in velocity for two bridle angles δ

This reel-in analytical solutions have been compared to the trajectories of the simulator. The values of the parameters used in the calculations are shown in Table 1, except that, according to previous discussion, we set $V_w = 0$, $\rho_T = 0$, $D_T = 0$. Two tests were carried out for bridle angles $\delta = 5°$ and $\delta = 25°$ and with reel-in velocities $v_{in} = -0.064$ and $v_{in} = -0.05$, respectively. Therefore, we considered reel-in velocities larger and smaller than the zero-tension velocity $v_{in}^* = -0.06$, but always in the side of the diagram that make the tether work under traction ($T > 0$) (see Fig. 4). We first verified with the code that the state vector $\boldsymbol{x}_{in} = [\hat{\boldsymbol{q}}_s \ \dot{\boldsymbol{q}}_s]$, with $\hat{\boldsymbol{q}}_s = [\gamma_1 \ 0 \ \theta \ 0 \ 0]^T$ and $\dot{\boldsymbol{q}}_s = \boldsymbol{0}$ and γ_1 and θ given by Eqs. (42)-(44), satisfies $\boldsymbol{f}(\boldsymbol{x}_{in}, \boldsymbol{u}) = 0$ for both δ values. In second place, we found the eigenvalues of the Jacobian matrix of $\boldsymbol{f}(\boldsymbol{x}, \boldsymbol{u})$ evaluated at $\boldsymbol{x}_{in}$. We found that both reel-in maneuvers are longitudinally unstable and the one with the higher δ was more unstable (the eigenvalue with positive real part was one order of magnitude larger). In third place, we integrate the equations of

24

motion numerically with initial conditions equal to $\boldsymbol{x}_{in}$ plus a small perturbation [see solid and blue lines in panels (a)-(c) in Fig. 5]. For convenience, the analytical solutions were plotted with dashed and red lines. In the case $(\delta, v_{in}) = (5°, -0.064)$, which is weakly unstable, the analytical and numerical solution practically overlaps in the plot (a zoom reveals that the distance among them increases slowly). For $(\delta, v_{in}) = (25°, -0.05)$ the instability is evident.

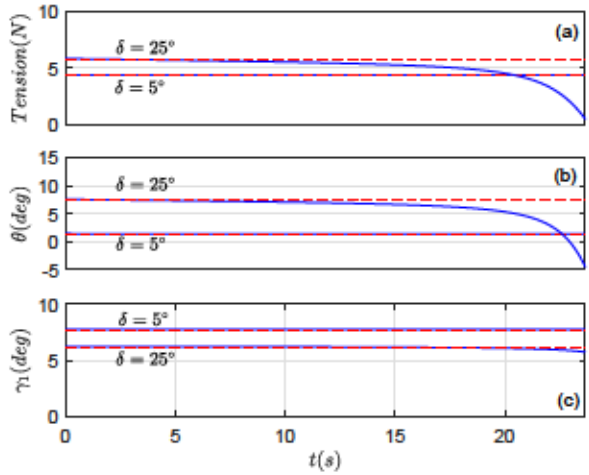

Figure 5: Panels (a) and (b) show the evolution of the tether tension, kite pitch angle and elevation angle, respectively for two reel-in maneuver with $(\delta, v_{in}) = (5°, \ 0.064)$ and $(\delta, v_{in}) = (25°, \ 0.05)$

5. Simulation results

This section presents two examples that illustrate the kind of dynamic analysis that can be carried out with the simulator. Quantitative results about energy generation were omitted because it is a topic beyond the scope of this work. It requires other tools such as optimal control solver, path planning, and a more accurate model for the aerodynamic performance of the rotors. Nevertheless, the analysis was split into ground and fly generation systems and we addressed open and close loop control problems. Additional results to the one presented in this section, such as 3D animations and more detailed information

25

about kite dynamics and the performance of the simulator, can be obtained by running the example programmes uploaded to the repository [30].

5.1. Ground-generation systems

During the energy generation phase of GG systems, the kite or drone performs a figure-of-eight trajectory while flying in crosswind conditions. As explained in the Introduction, this important maneuver has been studied in the past. However, to the best of our knowledge, it was never simulated with a self-consistent dynamical model because the control inputs did not correspond to the one that are present in a real AWE system. For this reason, we chose this maneuver and implemented an open-loop control strategy that ignores the reel-out of the main tether and changes the geometry of the bridle periodically. All the variables of $\boldsymbol{q}_c$ are constant, except for the bridle angle η, which follows the periodic law shown in Fig. 6a. The law has two constant phases of duration $1.2\sqrt{L_{T0}/g}$ and amplitude $\eta = 17.5^\circ$ and $\eta = -17.5^\circ$ linked by linear segments of duration $1.5\sqrt{L_{T0}/g}$. Therefore, the normalized period of the control law is $\tau_p = 5.4$.

For the physical parameters of Table 1 and the control law $\boldsymbol{q}_c(\tau)$ described in the paragraph above, one needs to compute the state $\boldsymbol{x}_0 = \boldsymbol{x}(\tau = 0)$ that, once used as initial condition in Eq. (41), gives a figure-of-eight trajectory $\boldsymbol{x}(\tau)$ satisfying $\boldsymbol{x}(0) = \boldsymbol{x}(\tau_p)$. This is, in principle, a difficult problem and it may even happen that such a periodic solution does not exist. In our case, the periodic solution exists and it was found by using a periodic orbit solver that also provides the stability of the trajectory (Floquet Multipliers) as a by-product [31]. As shown in Figs. 6 and 7, the calculations were carried out for several numbers of tether segments ($N_R = 1, 2$ and 3). The selected case is interesting from an academic point of view because it highlights the importance of tether flexibility. It is evident from Fig. 6b that a model with just a straight and rigid tether ($N_R = 1$) does not provide the correct result because it overestimates the minimum altitude of the trajectory. Calculations with $N_R = 2$ and $N_R = 3$ reveal that the flexibility of the tether make the kite fly at much less altitude

26

and it practically crashes. Interestingly, for this particular case, just few tether segments are enough to capture correctly the tether dynamics because increasing N_R beyond 3 does not change the trajectory significantly. The evolution of the Euler angles of the kite is smoother as the number of tether segments increases (see Fig. 7). We also mention that these orbits are unstable because they have a Floquet multiplier with modulus larger than one.

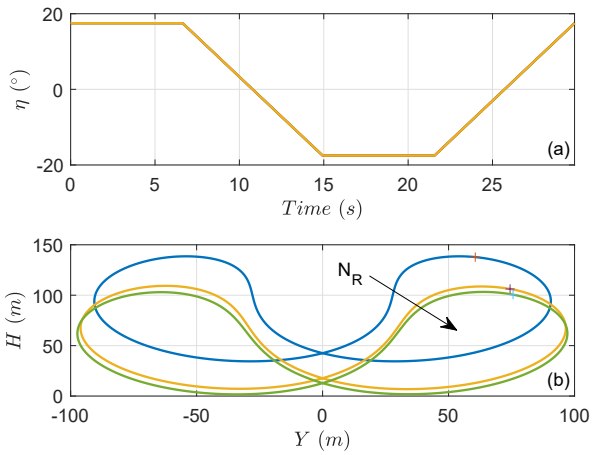

Figure 6: Panel (a) and (b) show the control law for η and the trajectory of the center of mass of the kite, respectively.

5.2. Fly-generation system

The last example involves a fixed-wing drone equipped with two rotors that spin in the same direction while generating power. The physical parameters of the mechanical system, which are shown in Table 2, do not coincide with any specific AWE system, but they mainly corresponds to the small glider Bubble Dancer, taken from the model provided by the AVL software [32]. We focus on a symmetric equilibrium state of the tethered drone with constant tether length and bridle geometry, and a rotor spinning velocity of $\Omega_G^* = 3500$ rpm or, in normalized form, $\dot{\lambda}_{1,2}^* = 6.4$. The state vector $\boldsymbol{x}^* = [\hat{\boldsymbol{q}}_s^* \;\; \dot{\boldsymbol{q}}_s^*]$ of such equilibrium

27

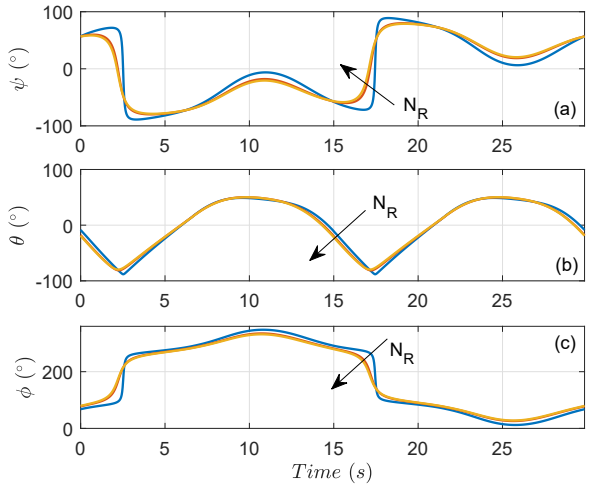

Figure 7: Evolution of Euler angles in the maneuver of Fig. 6.

state is

$$\hat{\boldsymbol{q}}_s^* = [\gamma_1^* \ \gamma_2^* \ \gamma_3^* \quad 0\ 0\ 0 \quad \theta^* \ 0 \ 0\ ] \tag{48}$$

$$\dot{\boldsymbol{q}}_s^* = \left[0 \quad 0 \quad 0 \quad 0\ 0\ 0 \quad 0 \quad 0\ 0 \quad \dot{\lambda}_1^* \ \dot{\lambda}_2^*\right] \tag{49}$$

One readily verifies that the equilibrium spinning velocity $\dot{\lambda}_{1,2}^*$ is achieved for a constant normalized motor torque of $\xi_1 = \xi_2 = 1.257 \times 10^{-4}$. Since both rotors spins with the same direction, a reaction torque acts on the drone and an aileron deflection is required to keep the system symmetric. Imposing the equilibrium condition $\boldsymbol{f}(\boldsymbol{x}^*, \boldsymbol{u}^*) = 0$ one finds the aileron deflection $\delta_a^* = -2.28°$, as well as the remaining state vector components $\gamma_1^* = 63.6°$, $\gamma_2^* = 66.4°$, $\gamma_3 = 69.3°$, $\theta^* = 7.9°$.

There are eigenvalues of the Jacobian matrix of the flow $\boldsymbol{f}$ evaluated at $\boldsymbol{x}^*$ with positive real parts. Therefore, the equilibrium state $\boldsymbol{x}^*$ is unstable. A numerical integration of Eq. (41) with initial condition equal to $\boldsymbol{x}^*$ plus a small perturbation confirms this result and shows that the drone moves laterally until it crashes. The equilibrium can be stabilized if the deflections of the control aerodynamic surfaces are no longer constant and they evolve according to the

28

	Symbol	Value	Symbol	Value
Environment	g	9.81 m/s^2	ρ	1.225 kg/m^3
	V_w	12 m/s		
Tether	L_{T0}	300 m	D_T	2 mm
	ρ_T	970 kg/m^3	$C_\perp$	1
Bridle	L_B	4 m	δ	60°
Kite	M_K	3.4 kg	S	13 m^2
	B	5 m	C	1.5 m
	I_{xx}	12.3 kgm^2	I_{yy}	3.2 kgm^2
	I_{zz}	11.4 kgm^2	I_{xz}	0.4 kg/m^2
	C_{x0}	-0.065	$C_{x\alpha}$	0.18
	$C_{y\beta}$	-1.57	C_{z0}	0.12
	$C_{z\alpha}$	-2.97	$C_{l\beta}$	1.24
	C_{lp}	-0.15	$C_{n\beta}$	0.78
	C_{nr}	-0.002	C_{m0}	0.13
	$C_{m\alpha}$	-0.76	C_{mq}	-0.17

Table 1: Parameters of the ground-generation system

following laws

$$\frac{d\delta_a}{d\tau} = -I_a\phi - P_a\dot{\phi} - D_a\ddot{\phi} \tag{50}$$

$$\frac{d\delta_r}{d\tau} = -I_r\psi - P_r\dot{\psi} - D_r\ddot{\psi} \tag{51}$$

$$\frac{d\delta_e}{d\tau} = I_e\left(\theta^* - \theta\right) \tag{52}$$

with $I_a = -I_r = 20$, $P_a = D_a = -P_r = -D_r = 10$, and $I_e = -10$, corresponding to the gains of a proportional-integral-derivative controller. Therefore, the deflection of the ailerons, the rudder, and the elevator for this close loop configuration depend on the attitude of the drone.

Figure 8 shows the evolution of the deflections of the control surfaces for a numerical simulation with initial conditions equal to $\boldsymbol{x}^*$ plus a perturbation. These control actions, which are all below few degrees, are enough to stabilize

29

the equilibrium state. As shown in Fig. 9 the Euler angles of the drone (solid lines) approach to the target trajectory $\boldsymbol{x}^*$ (red dashed lines). The state of the center of mass of the drone and the main tether (not shown) also approach to $\boldsymbol{x}^*$.

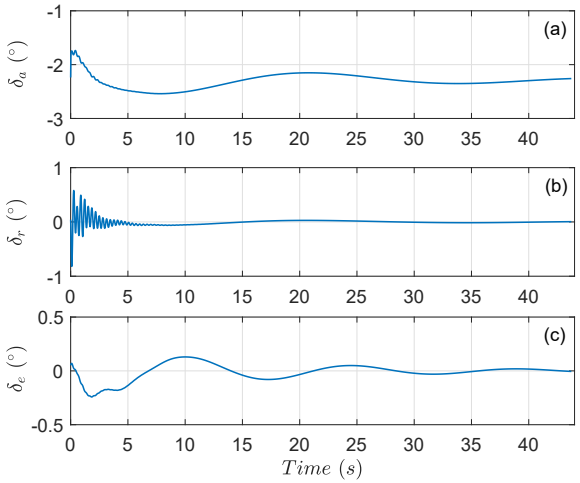

Figure 8: Panel (a), (b), and (c) show the evolution of the deflection of the control aerodynamic surfaces.

6. Conclusions

This work presents a flight simulator for a kite or drone equipped with rotors and linked to the ground by a single tether. The control vector of the simulator includes variables that are inputs in real AWE systems such as the lengths of the main tether and the lines of the bridle, the deflection of the aerodynamic control surfaces, and the torque of the motor controller of the rotors. The tether has been modeled by a chain of inelastic rods, thus eliminating the fast longitudinal waves of elastic tethers. This model setup, combined with the removal of the fast and cyclic angular coordinates of the rotors, yielded a non-stiff set of equations that allows numerical integrations with larger time steps. Important physical effects, some of them ignored frequently in AWE simulators, have been incorporated in the simulator. They include tether inertia, aerodynamic drag,

30

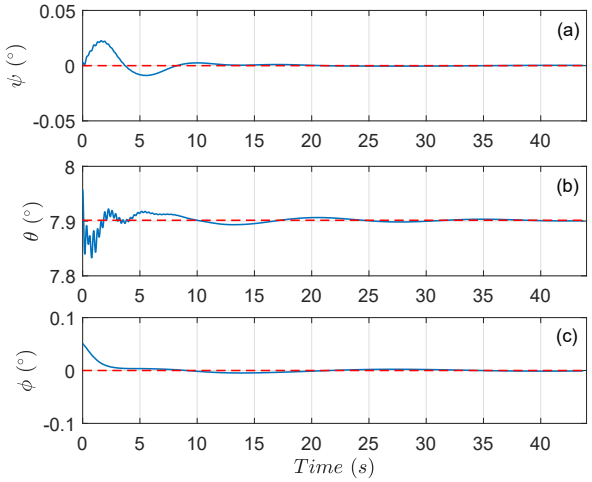

Figure 9: Solid lines in panels (a), (b), and (c) show the evolution of the yaw, pitch and roll angle, respectively. Dashed lines correspond to the target trajectory.

and flexibility as well as the dynamical effects that are consequence of the high spinning velocity of the rotors.

The lagrangian formalism, with a minimal coordinate approach, enhances the efficiency and robustness of the simulator due to several reasons. First, the dynamical system is a set of ordinary differential equations that is not coupled with nonlinear algebraic constraints. Moreover, all the tensors appearing in the equations were computed analytically and, since one of their indexes were directly related with the number of tether segments used to discretize the tether, their parallelization is straightforward and efficient. The good scalability of the code is evident from Fig. 2. The Lagrange formalism does also provides a bridge towards the hamiltonian formulation of the equations of motion. Although the evaluation of the right-hand-side of Hamilton's equations is a bit more demanding than Lagrange's equations (see Fig. 3), the numerical tests revealed that the numerical integration of Hamilton's equation is faster because the time step is larger for the same integrator tolerance.

The test cases carried out to verify the correct implementation of the simulator, and the results of Sec. 5 indicate that the code is versatile and useful

31

to investigate the dynamics of GG and FG AWE systems. Reel-in maneuvers, figure-of-eight trajectories and equilibrium state analysis were presented. Open and close-loop control strategies were implemented. However, quantitative results on energy generation would still need, in the view of the authors, an improvement of the aerodynamic model of the kite and the rotors, and the combination of the simulator with an optimal control software.

Acknowledgments

This work was supported by the Ministerio de Economía, Industria y Competitividad of Spain and the European Regional Development Fund under the project ENE2015-69937-R (MINECO/FEDER, UE). GSA work is supported by the Ministerio de Economía, Industria y Competitividad of Spain under the Grant RYC-2014-15357. RS was partially supported by the EU projects AWESCO (H2020-ITN-642682) and REACH (H2020- FTIPilot-691173).

Appendix A. Rotation matrices

The components of a vector in two different frames of reference, for instance $\boldsymbol{a} = a_{xA}\boldsymbol{x}_A + a_{yA}\boldsymbol{y}_A + a_{zA}\boldsymbol{z}_A = a_{xB}\boldsymbol{x}_B + a_{yB}\boldsymbol{y}_B + a_{zB}\boldsymbol{z}_B$, are related by a rotation matrix $\boldsymbol{R}^{AB}$ as $(a_{xA}, a_{yA}, a_{zA})^T = \boldsymbol{R}^{AB}\,(a_{xB}, a_{yB}, a_{zB})^T$. The rotation matrix that relates vector components in the Earth frame S_E and in a frame attached to tether segment i is

$$\boldsymbol{R}_i^{RE} = \begin{pmatrix} c\gamma_i c\varphi_i & c\gamma_i s\varphi_i & s\gamma_i \\ -s\varphi_i & c\varphi_i & 0 \\ -s\gamma_i c\varphi_i & -s\gamma_i s\varphi_i & c\gamma_i \end{pmatrix} \tag{A.1}$$

The rotation matrix for S_E and S_K is

$$\boldsymbol{R}^{EK} = \begin{pmatrix} c\psi c\theta & c\psi s\theta s\phi - s\psi c\phi & c\psi s\theta c\phi + s\psi s\phi \\ s\psi c\theta & s\psi s\theta s\phi + c\psi c\phi & s\psi s\theta c\phi - c\psi s\phi \\ -s\theta & c\theta s\phi & c\theta c\phi \end{pmatrix} \tag{A.2}$$

32

and the one relating vector components of S_{Gj} and S_K is

$$\boldsymbol{R}_j^{GK} = \begin{pmatrix} c\nu & 0 & -s\nu \\ s\nu s\lambda_j & c\lambda_j & c\nu s\lambda_j \\ s\nu c\lambda_j & -s\lambda_j & c\nu c\lambda_j \end{pmatrix} \tag{A.3}$$

Appendix B. Velocities and angular velocities of the solids

Appendix B.1. Kinematics of the tether segments

From the rotation matrix in Eq. (A.1), one finds the angular velocity of a segment i with respect to S_E

$$\boldsymbol{\omega}_{Ri} = \sin\gamma_i\dot{\varphi}_i\boldsymbol{x}_{Ri} - \dot{\gamma}_i\boldsymbol{y}_{Ri} + \cos\gamma_i\dot{\varphi}_i\boldsymbol{z}_{Ri} \tag{B.1}$$

Therefore, the components of the normalized angular velocity of segment i in S_i, $\boldsymbol{\omega}_{Ri} = p_{Ri}\boldsymbol{x}_{Ri} + q_{Ri}\boldsymbol{y}_{Ri} + r_{Ri}\boldsymbol{z}_{Ri}$, are

$$\begin{pmatrix} p_{Ri} \\ q_{Ri} \\ r_{Ri} \end{pmatrix} = \boldsymbol{W}_{Ri}\dot{\boldsymbol{q}}_{\boldsymbol{s}} \tag{B.2}$$

where the non-zero elements of $\boldsymbol{W}_{Ri}$ are

$$W_{Ri}(1, N_R + i) = s\gamma_i \tag{B.3}$$

$$W_{Ri}(2, i) = -1 \tag{B.4}$$

$$W_{Ri}(3, N_R + i) = c\gamma_i \tag{B.5}$$

The absolute normalized velocity of a segment i, found by taking the τ-derivative of Eq. (7), is

$$\begin{aligned} \boldsymbol{v}_{Ri} = &- \dot{l}_R \sum_{j=1}^{i} e_j \left[c\gamma_j \left(c\varphi_j\boldsymbol{x}_E + s\varphi_j\boldsymbol{y}_E\right) + s\gamma_j\boldsymbol{z}_E\right] \\ &+ l_R \sum_{j=1}^{i} e_j\dot{\gamma}_j \left[s\gamma_j \left(c\varphi_j\boldsymbol{x}_E + s\varphi_j\boldsymbol{y}_E\right) - c\gamma_j\boldsymbol{z}_E\right] \\ &+ l_R \sum_{j=1}^{i} e_j\dot{\varphi}_j c\gamma_j \left(s\varphi_j\boldsymbol{x}_E - c\varphi_j\boldsymbol{y}_E\right) \end{aligned} \tag{B.6}$$

33

After writing $\boldsymbol{v}_{Ri} = u_{Ri}\boldsymbol{x}_E + v_{Ri}\boldsymbol{y}_E + w_{Ri}\boldsymbol{z}_E$, one finds that Eq. (B.6) takes the form

$$\begin{pmatrix} u_{Ri} \\ v_{Ri} \\ w_{Ri} \end{pmatrix} = \boldsymbol{S}_{Ri}\dot{\boldsymbol{q}}_s + \boldsymbol{C}_{Ri}\dot{\boldsymbol{q}}_c \tag{B.7}$$

and the only non-zero elements of $\boldsymbol{S}_{Ri}$ and $\boldsymbol{C}_{Ri}$ are

$$S_{Ri}(:,j) = l_R e_j \left[\sin\gamma_j \cos\varphi_j \quad \sin\gamma_j \sin\varphi_j \quad -\cos\gamma_j\right]^T \tag{B.8}$$

$$S_{Ri}(:,N_R+j) = l_R e_j \left[\cos\gamma_j \sin\varphi_j \quad -\cos\gamma_j \cos\varphi_j \quad 0\right]^T \tag{B.9}$$

$$C_{Ri}(:,1) = -\sum_{j=1}^{i} e_j \left[\cos\gamma_j \cos\varphi_j \quad \cos\gamma_j \sin\varphi_j \quad \sin\gamma_j\right]^T \tag{B.10}$$

where the symbol : denotes that the indexes cover all the rows [from 1 to 3 in Eqs. (B.8)-(B.10)], $i = 1, \ldots, N_R$ and $e_j = 1$ ($e_j = 1/2$) if $j < i$ ($j = i$). In Eqs. (B.8)-(B.9), index j takes values $j = 1, \ldots, i$.

Appendix B.2. Kinematics of the kite

The normalized angular velocity of the kite with respect to S_E is found from the rotation matrix in Eq. (A.2). Its components in the S_K frame are

$$\begin{aligned} \boldsymbol{\omega}_K = &\left(\dot{\phi} - \dot{\psi}s\theta\right)\boldsymbol{x}_K + \left(\dot{\theta}c\phi + \dot{\psi}c\theta s\phi\right)\boldsymbol{y}_K + \\ &\left(\dot{\psi}c\theta c\phi - \dot{\theta}s\phi\right)\boldsymbol{z}_K \end{aligned} \tag{B.11}$$

or, writing $\boldsymbol{\omega}_K = p_K\boldsymbol{x}_K + q_K\boldsymbol{y}_K + r_K\boldsymbol{z}_K$,

$$\begin{pmatrix} p_K \\ q_K \\ r_K \end{pmatrix} = \boldsymbol{W}_K\dot{\boldsymbol{q}}_s \tag{B.12}$$

with the non-zero elements of $\boldsymbol{W}_K$ given by

$$W_K(:, 2N_R+1 : 2N_R+3) = \begin{pmatrix} 0 & -s\theta & 1 \\ c\phi & c\theta s\phi & 0 \\ -s\phi & c\theta c\phi & 0 \end{pmatrix} \tag{B.13}$$

34

The normalized absolute velocity of the kite is found by taking the τ-derivative of Eq. (13). It reads

$$\boldsymbol{v}_K = \frac{d\boldsymbol{r}_Q}{d\tau}\,|_{S_E} + \frac{1}{L_{T0}}\frac{d\overline{QO_K}}{d\tau}\,|_{S_K} + \boldsymbol{\omega_K} \times \frac{\overline{QO_K}}{L_{T0}} \tag{B.14}$$

where we used Coriolis Theorem. The kite velocity components in S_K, $\boldsymbol{v}_K = u_K\boldsymbol{x}_E + v_K\boldsymbol{y}_E + w_K\boldsymbol{z}_E$, are

$$\begin{pmatrix} u_K \\ v_K \\ w_K \end{pmatrix} = \boldsymbol{S}_K\dot{\boldsymbol{q}}_s + \boldsymbol{C}_K\dot{\boldsymbol{q}}_c \tag{B.15}$$

In order to find the non-zero elements of $\boldsymbol{S}_K$ and $\boldsymbol{C}_K$, we first note that the first term in Eq. (B.14) gives

$$S_K(:,j) = l_R\,[s\gamma_j c\varphi_j \quad s\gamma_j s\varphi_j \quad -c\gamma_j]^T \tag{B.16}$$

$$S_K(:,N_R+j) = l_R\,[c\gamma_j s\varphi_j \quad -c\gamma_j c\varphi_j \quad 0]^T \tag{B.17}$$

with $j = 1,\ldots,N_R$, and

$$C_K(:,1) = -\sum_{j=1}^{N_R}[c\gamma_j c\varphi_j \quad c\gamma_j s\varphi_j \quad s\gamma_j]^T \tag{B.18}$$

The second term in Eq. (B.14) only contributes to $\boldsymbol{C}_K$ with the non-zero elements

$$C_K(:,2:4) = \boldsymbol{R}^{EK}\cdot\begin{pmatrix} -c\delta c\eta & l_B s\delta c\eta & l_B c\delta s\eta \\ -c\delta s\eta & l_B s\delta s\eta & -l_B c\delta c\eta \\ -s\delta & -l_B c\delta & 0 \end{pmatrix}, \tag{B.19}$$

where the symbols $2:4$ denote that the indexes of $\boldsymbol{C}_K$ cover from its second to its fourth column. The last term in Eq. (B.14) gives

$$S_K(:,2N_R+1:2N_R+3) = -l_B\boldsymbol{R}^{EK} \cdot \begin{pmatrix} s\delta c\phi + c\delta s\eta s\phi & s\delta c\theta s\phi - c\delta s\eta c\theta c\phi & 0 \\ -c\delta c\eta s\phi & c\delta c\eta c\theta c\phi + s\delta s\theta & -s\delta \\ -c\delta c\eta c\phi & -c\delta s\eta s\theta - c\delta c\eta c\theta s\phi & c\delta s\eta \end{pmatrix} \tag{B.20}$$

35

Appendix B.3. Kinematics of the rotors

The components of the normalized angular velocities of the rotors in their own frames, $\boldsymbol{\omega}_{Gj} = p_{Gj}\boldsymbol{x}_{Gj} + q_{Gj}\boldsymbol{y}_{Gj} + r_{Gj}\boldsymbol{z}_{Gj}$, are written as

$$\begin{pmatrix} p_{Gj} \\ q_{Gj} \\ r_{Gj} \end{pmatrix} = \boldsymbol{W}_{Gj}\dot{\boldsymbol{q}}_s \tag{B.21}$$

with the non-zero elements of $\boldsymbol{W}_{Gj}$ given by

$$W_{Gj}(:, 2N_R + 1 : 2N_R + 3) = \boldsymbol{R}_j^{GK} \cdot W_K(:, 2N_R + 1 : 2N_R + 3) \tag{B.22}$$

$$W_{Gj}(1, 2N_R + 3 + j) = 1 \tag{B.23}$$

After using Coriolis Theorem, the normalized velocities of the centers of mass of the rotors with respect to S_E becomes

$$\boldsymbol{v}_{Gj} = \boldsymbol{v}_K + \boldsymbol{\omega}_K \times \frac{\overline{O_K O_{Gj}}}{L_{T0}} \tag{B.24}$$

where we took into account that the derivative of $\overline{O_K O_{Gj}}$ for an observer linked to the kite is zero. After writing $\boldsymbol{v}_{Gj} = u_{Gj}\boldsymbol{x}_E + v_{Gj}\boldsymbol{y}_E + w_{Gj}\boldsymbol{z}_E$, one finds

$$\begin{pmatrix} u_{Gj} \\ v_{Gj} \\ w_{Gj} \end{pmatrix} = \boldsymbol{S}_{Gj}\dot{\boldsymbol{q}}_s + \boldsymbol{C}_{Gj}\dot{\boldsymbol{q}}_c \tag{B.25}$$

where $\boldsymbol{S}_{Gj} = \boldsymbol{S}_K + \boldsymbol{S}_{Gj}^0$, $\boldsymbol{C}_{Gj} = \boldsymbol{C}_K$, and the non-zero elements of $\boldsymbol{S}_{Gj}^0$ are

$$S_{Gj}^0(:, 2N_R + 1 : 2N_R + 3) = \boldsymbol{R}^{EK} \cdot \begin{pmatrix} z_{Gj}c\phi + y_{Gj}s\phi & z_{Gj}c\theta s\phi - y_{Gj}c\theta c\phi & 0 \\ -x_{Gj}s\phi & x_{Gj}c\theta c\phi + z_{Gj}s\theta & -z_{Gj} \\ -x_{Gj}c\phi & -y_{Gj}s\theta - x_{Gj}c\theta s\phi & y_{Gj} \end{pmatrix} \tag{B.26}$$

Appendix C. Aerodynamic models

Appendix C.1. Aerodynamic model of the tether

The simulator considers the aerodynamic force component normal to each tether segment and ignores the tangential force component and the aerodynamic

36

torque. The dimensionless aerodynamic force acting on a segment i is

$$\boldsymbol{f}_{Ri} = -\chi_R l_R v^A_{Ri\perp} \boldsymbol{v}^A_{Ri\perp} \tag{C.1}$$

where we introduced the coefficient $\chi_R \equiv C_\perp \rho D_t L_{t0}^2/2M_K$, air density ρ, tether diameter D_t, normal drag coefficient $C_\perp$, and the normalized perpendicular airspeed

$$\boldsymbol{v}^A_{Ri\perp} = \boldsymbol{v}^A_{Ri} - \left(\boldsymbol{v}^A_{Ri} \cdot \boldsymbol{x}_{Ri}\right) \boldsymbol{x}_{Ri} \tag{C.2}$$

with $\boldsymbol{v}^A_{Ri} = \boldsymbol{v}_{Ri} - \boldsymbol{v}_w$ being the normalized airspeed of a tether segment.

Appendix C.2. Aerodynamic model of the kite

The normalized aerodynamic force of the kite and the moment about its center of mass are given by

$$\begin{aligned}
\boldsymbol{f}_K =& \mu \left(v^A_K\right)^2 \left[\left(C_{x0} + C_{x\alpha}\alpha\right) \boldsymbol{x}_K + \left(C_{y\beta}\beta + C_{y\delta_r}\delta_r\right) \boldsymbol{y}_K \right. \\
&\left. + \left(C_{z0} + C_{z\alpha}\alpha\right) \boldsymbol{z}_K\right], \qquad \text{(C.3)} \\
\boldsymbol{m}_K =& \mu \left(v^A_K\right)^2 \epsilon_b \left[\left(C_{l\beta}\beta + C_{lp}p + C_{l\delta_a}\delta_a + C_{l\delta_r}\delta_r\right) \boldsymbol{x}_K \right. \\
&\left. + \left(C_{n\beta}\beta + C_{nr}r + C_{n\delta_r}\delta_r\right) \boldsymbol{z}_K\right] \\
&\mu \left(v^A_K\right)^2 \epsilon_c \left(C_{m0} + C_{m\alpha}\alpha + C_{mq}q + C_{m\delta_e}\delta_e\right) \boldsymbol{y}_K \qquad \text{(C.4)}
\end{aligned}$$

with $\boldsymbol{v}^A_K = \boldsymbol{v}_K - \boldsymbol{v}_w$ the airspeed of the kite, $\mu \equiv \rho S L_{T0}/2M_K$, $\epsilon_b = B/L_{T0}$, $\epsilon_c = C/L_{T0}$, $(p, q, r) \equiv \sqrt{g/L_{T0}}(Bp_K/2, Cq_K, Br_K/2)/V_T$, and V_T a reference velocity. For simplicity, the effect of the control aerodynamic surfaces (ailerons, elevator and rudder) was included in the aerodynamic torque but it was ignored in the force except for the lateral force of the rudder deflection. The attack and sideslip angles of the kite in Eqs. (C.3) and (C.4) are given by

$$\alpha = \arctan\left(\frac{\boldsymbol{v}^A_K \cdot \boldsymbol{z}_K}{\boldsymbol{v}^A_K \cdot \boldsymbol{x}_K}\right), \quad \beta = \arcsin\left(\frac{\boldsymbol{v}^A_K \cdot \boldsymbol{y}_K}{|\boldsymbol{v}^A_K|}\right). \tag{C.5}$$

Appendix C.3. Aerodynamic model of the rotors

The simulator only includes the aerodynamic force and torque components along the axes of the rotors ($\boldsymbol{x}_{Gi}$). The model is based on the airspeed normal

37

to the plane of the blade, $v^A_{Gi\perp} = \boldsymbol{v}^A_{Gi} \cdot \boldsymbol{x}_{Gi}$. The dimensionless force and torque are

$$\boldsymbol{f}^i_{AG} = -\chi_G C_{fi} \left(v^A_{Gi\perp}\right)^2 \boldsymbol{x}_{Gi} \tag{C.6}$$

$$\boldsymbol{m}^i_{AG} = l_G \chi_G C_{mi} \left(v^A_{Gi\perp}\right)^2 \boldsymbol{x}_{Gi} \tag{C.7}$$

where $\boldsymbol{v}^A_{Gi} = \boldsymbol{v}_{Gi} - \boldsymbol{v}_w$ is the airspeed of rotor i, and $\chi_G \equiv \rho\pi R^2_G L_{T0}/2M_K$. In general, the thrust and moment coefficients, C_f and C_m of a rotor named j depend on its tip speed ratio and the pitch angle if there is a controller. For certain regimes, C_{fi} and C_{mi} are both positive and the rotor gives power and a drag. For others, the rotor acts as a propeller and gives thrust while consuming power ($C_{fi} < 0$ and $C_{mi} < 0$). Since there is a lack of information on the performance of the rotors used by AWES, our simulator takes constant values for C_{fi} and C_{mi}.

References

[1] A. Cherubini, A. Papini, R. Vertechy, M. Fontana, Airborne wind energy systems: A review of the technologies, Renewable and Sustainable Energy Reviews 51 (2015) 1461 – 1476. doi:https://doi.org/10.1016/j.rser.2015.07.053.

[2] M. Diehl, R. Leuthold, R. Schmehl (Eds.), The International Airborne Wind Energy Conference 2017: Book of Abstracts, Freiburg, Germany, 2017. doi:10.6094/UNIFR/12994.

[3] C. Sieg, T. Gehrmann, P. Bechtle, U. Zillmann, Awesome: An affordable standardized open-source test platform for awe systems, in: M. Diehl, R. Leuthold, R. Schmehl (Eds.), Book of Abstracts of the International Airborne Wind Energy Conference 2017, Albert Ludwig University Freiburg and Delft University of Technology, Freiuburg, Germany, 2017, pp. 1–188. doi:10.4233/uuid:4c361ef1-d2d2-4d14-9868-16541f60edc7.

[4] M. Winter, E. Schmidt, R. Silva de Oliveira, An open-source software platform for awe systems, in: M. Diehl, R. Leuthold, R. Schmehl (Eds.), Book of Abstracts of the International Airborne Wind Energy Conference 2017, Albert Ludwig University Freiburg and Delft University of Technology, Freiuburg, Germany, 2017, pp. 1–188. doi:10.4233/uuid:4c361ef1-d2d2-4d14-9868-16541f60edc7.

[5] U. Fechner, R. van der Vlugt, E. Schreuder, R. Schmehl, Dynamic model of a pumping kite power system, Renewable Energy 83 (2015) 705 – 716. doi:http://dx.doi.org/10.1016/j.renene.2015.04.028.

[6] A. Okholm, Kite energy simulator, https://github.com/kitextech/kitesim (2017).

[7] U. Fechner, A methodology for the design of kite-power control systems, Ph.D. thesis, Delft University of Technology, Delft, The Netherland (November 2016). doi:10.4233/uuid:85efaf4c-9dce-4111-bc91-7171b9da4b77.

[8] M. L. Loyd, Crosswind kite power, J. Energy 4 (3) (1980) 24–30. doi:10.2514/3.48021.

[9] M. S. Ahmed, A. Hably, S. Bacha, Kite generator system modeling and grid integration, IEEE Transactions on Sustainable Energy 4 (4) (2013) 968–976. doi:10.1109/TSTE.2013.2260364.

[10] L. Fagiano, A. Zgraggen, M. Morari, M. Khammash, Automatic crosswind flight of tethered wings for airborne wind energy: Modeling, control design, and experimental results, Control Systems Technology, IEEE Transactions on 22 (4) (2014) 1433–1447. doi:10.1109/TCST.2013.2279592.

[11] A. Ilzhfer, B. Houska, M. Diehl, Nonlinear mpc of kites under varying wind conditions for a new class of large-scale wind power generators, International Journal of Robust and Nonlinear Control 17 (17) (2007) 1590–1599. doi:10.1002/rnc.1210.

[12] G. Sánchez-Arriaga, Dynamics and control of single line kites, The Aeronautical Journal 110 (1111) (2006) 615–621. doi:10.1017/S0001924000001470.

[13] E. Terink, J. Breukels, R. Schmehl, W. Ockels, Flight dynamics and stability of a tethered inflatable kiteplane, AIAA Journal of Aircraft 48 (2) (2011) 503–513. doi:10.2514/1.C031108.

[14] L. Salord Losantos, G. Sánchez-Arriaga, Flight dynamics and stability of kites in steady and unsteady wind conditions, Journal of Aircraft 52 (2) (2015) 660–666. doi:10.2514/1.C032825.

[15] A. Pastor-Rodríguez, G. Sánchez-Arriaga, M. Sanjurjo-Rivo, Modeling and stability analysis of tethered kites at high-altitudes, Journal of Guidance, Control, and Dynamics 40 (8) (2017) 1892–1901. doi:10.2514/1.G002550.

[16] S. G. C. de Groot, J. Breukels, R. Schmehl, W. Ockels, Modeling kite flight dynamics using a multibody reduction approach, Journal of Guidance, Control and Dynamics 34 (6) (2011) 1671–1682. doi:10.2514/1.52686.

[17] F. Gohl, R. H. Luchsinger, Simulation Based Wing Design for Kite Power, Springer Berlin Heidelberg, Berlin, Heidelberg, 2013, pp. 325–338. doi:10.1007/978-3-642-39965-7_18.

[18] P. Williams, B. Lansdorp, W. Ockels, Nonlinear control and estimation of a tethered kite in changing wind conditions, Journal of Guidance, Control and Dynamics 31 (3) (2008) 793–799. doi:10.2514/1.31604.

[19] M. Zanon, S. Gros, J. Andersson, M. Diehl, Airborne wind energy based on dual airfoils, IEEE Transactions on Control Systems Technology 21 (4) (2013) 1215–1222. doi:10.1109/TCST.2013.2257781.

[20] V. Beletsky, E. Levin, A. A. Society, Dynamics of space tether systems, Advances in astronautical sciences, Published for the American Astronautical Society by Univelt, Inc., 1993.

[21] J. Peláez, O. López-Rebollal, E. Lorenzini, M. L. Cosmos, Two-bar model for the dynamics and stability of electrodynamic tethers, Journal of Guidance, Control, and Dynamics 25 (6) (2002) 1125–1135. doi:10.2514/2.4992.

[22] J. Puig-Suari, J. M. Logunski, S. G. Tragesser, Aerocapture with a flexible tether, Journal of Guidance Control Dynamics 18 (1995) 1305–1312. doi:10.2514/3.21546.

[23] B. L. Biswell, J. Puig-Suari, J. M. Longuski, S. G. Tragesser, Three-Dimensional Hinged-Rod Model for Elastic Aerobraking Tethers, Journal of Guidance Control Dynamics 21 (1998) 286–295. doi:10.2514/2.4234.

[24] R. A. Adomaitis, Kites and bifurcation theory, SIAM Review 31 (3) (1989) 478. doi:10.1137/1031092.

[25] P. Williams, B. Lansdorp, W. Ockels, Optimal crosswind towing and power generation with tethered kites, Journal of Guidance, Control and Dynamics 31 (1) (2008) 81–93. doi:10.2514/1.30089.

[26] J. Alonso-Pardo, G. Sanchez-Arriaga, Kite model with bridle control for wind-power generation, Journal of Aircraft 52 (3) (2015) 917–923. doi:10.2514/1.C033283.

[27] G. Sánchez-Arriaga, M. Garcia-Villalba, R. Schmehl, Modelling and dynamics of a two-line kite, Applied Mathematical Modelling 47 (2017) 473–486. doi:https://doi.org/10.1016/j.apm.2017.03.030.

[28] A. P. Minakov, Fundamentals of the thread mechanics, Proceedings of the Moscow Textile Institute 9 (1941).

[29] G. Sánchez-Arriaga, A. Pastor-Rodrguez, R. Borobia-Moreno, R. Schmehl, A constraint-free flight simulator package for airborne wind energy systems, Journal of Physics: Conference Series 1037 (6) (2018) 062018.
URL http://stacks.iop.org/1742-6596/1037/i=6/a=062018

[30] G. Sánchez-Arriaga, A. Pastor-Rodríguez, Kiteflex, https://github.com/apastor3/laksa (2018).

[31] M. Lara, J. Peláez, On the numerical continuation of periodic orbits. an intrinsic, 3-dimensional, differential, predictor-corrector algorithm, Astronomy and Astrophysics 389 (2002) 692–701. doi:10.1051/0004-6361:20020598.

[32] M. Drela, H. Youngren, Avl: Athena vortex lattice, http://web.mit.edu/drela/Public/web/avl/ (1988).

	Symbol	Value	Symbol	Value
Environment	g	9.81 m/s^2	ρ	1.225kg/m^3
	V_w	7 m/s		
Tether	N_R	3		
	L_{T0}	30 m	D_T	2 mm
	ρ_T	970 kg/m^3	$C_\perp$	1
Bridle	L_B	3 m	δ	80°
	η	0		
Drone	M_K	2 kg	S	0.75 m^2
	B	3 m	C	0.25 m
	I_{xx}	0.2 kgm^2	I_{yy}	0.078 kgm^2
	I_{zz}	0.28 kgm^2	I_{xz}	-0.002 kgm^2
	C_{x0}	-0.025	$C_{x\alpha}$	0.67
	$C_{y\beta}$	-0.4	C_{z0}	-0.91
	$C_{z\alpha}$	-5.65	$C_{l\beta}$	-0.26
	C_{lp}	-0.2	$C_{n\beta}$	0.052
	C_{nr}	-0.02	C_{m0}	0.074
	$C_{m\alpha}$	-0.86	C_{mq}	-0.3
	$C_{l\delta_a}$	0.055	$C_{l\delta_r}$	0.0033
	$C_{n\delta_r}$	-0.046	$C_{m\delta_e}$	-1.54
	$C_{y\delta_r}$	0.2		
Rotors	N_G	2		
	M_G	0.3 kg	R_G	0.2 m
	ν	0	X_G	0.125 m
	Y_G	0.75 m	Z_G	0
	C_f	0.08	C_m	0.1

Table 2: Parameters of the fly-generation system.